



AIAA-2003-3613

Simultaneous High-resolution Optical Wavefront and Flow Diagnostics for High-speed Flows

B. Thurow, M. Samimy and W. Lempert
Gas Dynamics and Turbulence Laboratory
The Ohio State University

S.R. Harris
Air Force Research Laboratory, Sensors Directorate

J. Widiker and B. Duncan
University of Dayton

**34th AIAA Plasmadynamics and Lasers
Conference**

23-26 June, 2003/ Orlando, FL

Report Documentation Page				Form Approved OMB No. 0704-0188	
Public reporting burden for the collection of information is estimated to average 1 hour per response, including the time for reviewing instructions, searching existing data sources, gathering and maintaining the data needed, and completing and reviewing the collection of information. Send comments regarding this burden estimate or any other aspect of this collection of information, including suggestions for reducing this burden, to Washington Headquarters Services, Directorate for Information Operations and Reports, 1215 Jefferson Davis Highway, Suite 1204, Arlington VA 22202-4302. Respondents should be aware that notwithstanding any other provision of law, no person shall be subject to a penalty for failing to comply with a collection of information if it does not display a currently valid OMB control number.					
1. REPORT DATE JUN 2003		2. REPORT TYPE		3. DATES COVERED 00-00-2003 to 00-00-2003	
4. TITLE AND SUBTITLE Simultaneous High-resolution Optical Wavefront and Flow Diagnostics for High-speed Flows				5a. CONTRACT NUMBER	
				5b. GRANT NUMBER	
				5c. PROGRAM ELEMENT NUMBER	
6. AUTHOR(S)				5d. PROJECT NUMBER	
				5e. TASK NUMBER	
				5f. WORK UNIT NUMBER	
7. PERFORMING ORGANIZATION NAME(S) AND ADDRESS(ES) Ohio State University, Department of Mechanical Engineering, Columbus, OH, 43210				8. PERFORMING ORGANIZATION REPORT NUMBER	
9. SPONSORING/MONITORING AGENCY NAME(S) AND ADDRESS(ES)				10. SPONSOR/MONITOR'S ACRONYM(S)	
				11. SPONSOR/MONITOR'S REPORT NUMBER(S)	
12. DISTRIBUTION/AVAILABILITY STATEMENT Approved for public release; distribution unlimited					
13. SUPPLEMENTARY NOTES					
14. ABSTRACT					
15. SUBJECT TERMS					
16. SECURITY CLASSIFICATION OF:			17. LIMITATION OF ABSTRACT Same as Report (SAR)	18. NUMBER OF PAGES 18	19a. NAME OF RESPONSIBLE PERSON
a. REPORT unclassified	b. ABSTRACT unclassified	c. THIS PAGE unclassified			

Simultaneous High-resolution Optical Wavefront and Flow Diagnostics for High-speed Flows

Brian Thurow, Mo Samimy¹ and Walter Lempert
Gas Dynamics and Turbulence Laboratory
The Ohio State University

Scott Harris
Air Force Research Laboratory – Sensors Directorate

Jeff Widiker and Bradley Duncan
University of Dayton

Simultaneous high spatial-resolution flow visualization and wavefront sensing are used to investigate the optical aberrations that occur due to a compressible shear layer. A preliminary model is developed to relate flow visualization images with wavefronts measured using a Shack-Hartmann wavefront sensor. Initial results are quite encouraging as a comparison between the Shack-Hartmann measured wavefronts and wavefronts produced by applying the model to flow visualization images produces correlation levels well above 0.7. Future work will incorporate a more realistic geometry to further develop the model and investigate the effects of individual large-scale structures on wavefront distortion with more detail.

I. Introduction

The field of aero-optics has received increased attention over the last few years as the application of lasers onboard aircrafts has increased. Lasers are progressively being more used in various systems such as directed energy weapons, missile guidance and radar. It is well known, however, that the performance of these systems is ultimately limited by the interaction of the optical wavefront entering/exiting the aircraft with the turbulent flow surrounding the aircraft. The study of this interaction is termed aero-optics (also referred to as fluid-optics interaction).

The flow field around a tactical aircraft is highly turbulent and compressible. As the index-of-refraction in air is proportional to its density, density gradients within the flow field lead to a distortion of the wavefront as it passes through the flow. The distortion takes the form of a spatially varying optical phase across the aperture of the beam and can lead to decreased intensity of the beam at the target (measured by Strehl ratio), beam steering, defocus, and image blurring. For the flow over an aircraft, the variation in

time can be on the order of 10's to 100's of kHz. As a result, currently available adaptive-optic techniques cannot measure and correct for the distortion in real-time.

As discussed in a review article by Jumper and Fitzgerald (2001), up until the early 1990s, the lack of ability to investigate phenomena at these high frequencies greatly limited further advances in the field. Recent advances in experimental diagnostics, however, have opened the door for a renewed effort to understand the aero-optical problems associated with compressible turbulent flows. For example, the small aperture beam technique (SABT) has been developed and used (e.g., Hugo et al. 1997 or Jumper and Fitzgerald, 2001) to measure time-resolved, one-dimensional wavefronts within a weakly compressible shear layer. Outside of this line of work, however, temporally resolved data has been limited to single point or numerical measurements.

One recent advance in high-speed experimental diagnostics with potential use for aero-optics research is the development and application of a pulse burst laser system that can produce between 1 and 99 laser pulses at a rate up to 1 MHz. Used in conjunction with a high-speed digital camera, the pulse burst laser system at The Ohio State University (one of only two such systems) has been developed into a planar flow visualization technique that can capture a sequence of 17 two-dimensional images over a span of ~100 microseconds. The increased capabilities of this high-speed imaging technique over that of traditional

¹Corresponding author: Samimy.1@osu.edu

techniques has been successfully demonstrated in the exploration of characteristics and convective velocities of large-scale turbulence structures at varying degrees of compressibility (Thurow et al. 2002 and 2003c) as well as the identification of instantaneous noise sources of jets (Hileman et al., 2002). Currently, work is under way to further develop the technique into a temporally resolved quantitative technique based on planar Doppler velocimetry (Thurow et al., 2003).

In addition, progress in polymer lenslet array and CCD technologies have allowed for advances in wavefront diagnostics, specifically the development of high-speed Shack-Hartmann wavefront sensors. The Sensors Directorate of the Air Force Research Laboratory (AFRL/SN), in conjunction with the University of Dayton (UD), have developed such a sensor for use in studying optical aberrations induced by turbulent flows. By trading-off resolution sample size their SH is capable of capturing 28 frames at 1 MHz, allowing it to be used to obtain simultaneous measurements with OSU's flow diagnostic equipment previously mentioned (Thurow et al., 2003a).

In parallel with these advances in experimental diagnostics, the field of flow control has experienced a renewed vigor with the development of high-frequency fluidic actuators that have the ability to provide both high-frequency and high-amplitude forcing of a flow. Up until recently, flow control researchers have had to trade off high frequencies with high amplitudes. Kastner and Samimy (2002, 2003), for example, have developed, characterized and demonstrated the use of Hartmann fluidic actuators for high-speed flow control. These actuators can operate in the 1-10 kHz range with relatively high energy. These actuators have already exhibited the ability to control (or regulate) large scale structures within cavity flows (Stanek et al., 2002; Raman & Kibens, 2002), impinging jets (Kastner and Samimy 2003), and are currently being developed for other flow applications.

These recent advances in the fields of optical diagnostics and flow control are highly complementary for the field of aero-optics. The MHz rate flow visualization system has proven useful for understanding the dynamics of turbulence structures. Coupled with wavefront diagnostic techniques, such as the Shack-Hartmann (SH) wavefront sensor used in this study, the potential exists to correlate features of the flow with features contained in the aberrated optical wavefront. Flow control using high frequency and amplitude fluidic actuators, for example, can be used to manipulate turbulence structures. This can serve two purposes. One, it can be used to change the properties of structures in order to gauge their effect on the wavefront. Second, once the effect of structures is better understood, flow control can be adapted to practical applications to produce a flow with minimal

wavefront distortion. Thus, optical diagnostics and flow control can be used hand-in-hand to tackle problems associated with aero-optics.

Due to the potential application of these techniques to the field of aero-optics, a research effort has been started to explore how MHz rate flow diagnostics can be applied with respect to the optical distortion that occurs within a shear layer. This effort has led to an earlier conference publication (Thurow et al., 2003) and the current work.

Previous Work

A precursor to the current work was presented earlier this year (Thurow et al., 2003a). In this earlier work, the pulse burst laser was used for MHz rate flow visualization and a Shack-Hartmann (SH) sensor was developed and used to measure the optical wavefront of a beam passing through the flow at rates up to 1 MHz. The intention of this earlier work was simply to demonstrate MHz rate capabilities with respect to aero-optics and to begin development of the processes. The knowledge gained from this preliminary study was quite encouraging and demonstrated a large amount of potential for time-resolved wavefront data.

In these experiments, flow visualization and wavefront sensing (through the SH sensor) were used simultaneously on the flow field of a Mach 1.3 rectangular jet. This flow field was chosen simply due to its ease for flow visualization and compatibility with existing facilities. As such, it was not intended to represent a practical geometry. The results of this work demonstrated the ability to simultaneously perform flow and wavefront diagnostics on the same flow field. The flow visualization system captured two dimensional images of the flow correlated in time while the MHz rate SH sensor produced two-dimensional wavefronts correlated in time.

While the flow visualization system had been developed and used in other applications, the MHz rate SH sensor was designed and used for the very first time. One shortcoming to this initial effort, however, was the lack of additional diagnostic tools to compare the results with. As part of this initial effort, a very simple and preliminary model was also developed to describe the flow field's influence on the optical wavefront. The model had moderate success in its ability to match features of the flow with features of the distorted wavefronts. This was quite encouraging considering the simplicity of the model and the very preliminary nature of the MHz rate SH sensor. More detailed analysis concerning the accuracy of the model or the SH sensor, however, was beyond the scope of these preliminary experiments. The extension of this work is the subject of the current paper.

Current Work

The current work seeks to address some of the issues discussed in the previous work by implementing some more traditional optical techniques in a study of the same flow field. A high resolution, single-shot Shack-Hartmann wavefront sensor is used to measure optical wavefronts and a high resolution, single-shot pulsed laser/camera is used to acquire images of the flows. Although lacking the time information of the previous work, this data provides a more accurate and detailed look at the flow field and its associated optical distortion. The data also provides a good basis for comparison when extending the techniques into the real-time domain.

II. Experimental diagnostics

Two diagnostics techniques are combined and used to explore the effects of turbulence on an optical wavefront passing through the flow. For flow diagnostics, non-intrusive planar flow visualization is used to get an image of the mixing layer of the flow. For wavefront diagnostics, a Shack-Hartmann wavefront sensor is used to measure the spatially varying phase of an optical wavefront passing through the flow. These techniques are discussed in a general fashion below.

A. Planar Flow Visualization

For flow visualization, a pulsed Nd:YAG laser beam is formed into a thin sheet and directed through a plane in the flow field. Scattered laser light from particles contained in the flow is then captured using a CCD camera. In this set of experiments, seeding is provided using the product formation technique where water vapor contained in the warm moist ambient air condenses into nanometer-scale droplets upon entrainment into the jet and mixing with the cold and dry jet core air. Concerns about the size of the particles formed and their response time have been previously addressed, and the particles are believed to accurately mark the features of the flow (Elliott et al., 1992).

The advantage of this method of flow visualization is its simplicity and ability to mark the most dominant features within the mixing layer (i.e. large-scale structures). The technique gives a very good qualitative impression of the dynamics within the mixing layer. The disadvantage of the technique, however, is the limited amount of quantitative information that can be extracted. The intensity of the scattered laser light is directly proportional to the number density and size of water droplets contained within a given volume of the flow. The number density and size of particles, however, is a complex function of

mixture fraction, density, temperature and time. Due to this complex process, it is quite difficult to extract further information from images beyond the simple assessment that significant mixing has occurred where there is signal. Despite these limitations, the technique has been successfully used in a number of studies of compressible flows.

In the context of aero-optics, there might be an additional concern about the influence of water particles on the optical wavefront passing through the mixing layer. The effect on the wavefront, however, is thought to be minimal as the particles are very small and the scattering is close to Rayleigh scattering regime. Furthermore, the particle number density is quite small compared to the number density of air molecules (<1%). Thus, the amount of light scattered towards the Shack-Hartmann sensor by the water particles will be orders of magnitude smaller than the light directly falling onto the SH sensor.

B. Shack-Hartmann wavefront sensor

Two-dimensional optical wavefronts can be measured using a Shack-Hartmann wavefront sensor (subsequently called a SH sensor). The SH sensor operates on the principle that the focal point of light will shift in space depending upon the incident wavefront's tilt. This is demonstrated in Figure 1 and described by

$$\theta \approx \tan \theta = \frac{\delta}{f} \quad (1)$$

where θ is the angle of the incident wavefront, δ is the displacement of the focused spot and f is the focal length of the lens. By placing a CCD camera at the focal plane of the lens, the location of the spot can be recorded and the average wavefront tilt over the aperture determined.

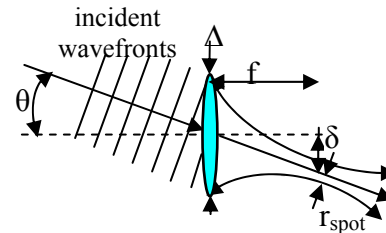


Figure 1 - Schematic of wavefront tilt measurement

A SH sensor uses an array of lenses (lenslet array) to measure the tilt of the wavefront at a number of discrete locations. If the spatial sampling of the wavefront is sufficiently fine such that the wavefront is approximately linear within each sampled area, an array of diffraction limited spots will be produced by the lenslet array. The array of spots can then be recorded by a CCD camera. The associated spot displacements can

then be measured directly from the recorded spot pattern. A more detailed analysis of SH sensors with respect to the current application can be found in Thurow et al. (2003a).

The advantage of a SH sensor is its ability to measure wavefront distortion directly as opposed to measuring an artifact of the distortion (e.g. the point spread function of a beam passing through the flow). A SH sensor's response is independent of the incident wavelength of light. Therefore, the laser chosen to produce the incident wavefront, which ideally is planar (i.e. spatially filtered), can be chosen according to the experiment and does not have to be chosen to coincide with the laser to be used onboard the aircraft. As such, we are able to use an Nd:YAG laser at 532 nm, although the laser onboard the Boeing airborne laser, for example, operates at 1315 nm.

III. Experimental equipment and set-up

A. Flow field

The flow field for this study is a Mach 1.3 rectangular jet. This flow field was chosen simply due to its compressible nature, ease for flow visualization, and compatibility with existing facilities. As such, it was not intended to represent a practical geometry. [A new facility is currently being designed with a more aero-optics applicable geometry]. The nozzle's contour was designed for Mach 1.3 using the method of characteristics to provide uniform flow at the nozzle exit, which has dimensions of 3.81 x 1.27 cm (1.5 x 0.5 in.). It has a measured Mach number of 1.28. Air is supplied to the stagnation chamber from two four-stage compressors; it is filtered, dried and stored in two cylindrical tanks with a total capacity of 42.5 m³ at 16.5 MPa (1600 ft³ at 2500 psi). Assuming isentropic expansion, the jet density is 1.57 kg/m³ and the ambient air density is 1.18 kg/m³.

B. Single-shot, high-resolution flow visualization

For high-resolution flow visualization, a frequency-doubled, pulsed Nd:YAG laser was used to illuminate the flow field. The laser was manufactured by Spectra-Physics (PRO-250-10) and can produce a single 10 nsec laser pulse with energy up to 750 mJ/pulse at 532 nm; only ~2 mJ was required for these experiments. The laser has a repetition rate of 10 Hz. Seed particles were introduced into the flow via product formation, as described earlier. Images were acquired using a PixelVision CCD camera with 1024 x 1024 resolution and 16-bit precision output. The large dynamic range allows for a finer distinction between mixed and unmixed fluid interfaces.

C. Single-shot, high-resolution Shack Hartmann wavefront sensor

The high resolution SH sensor used the same laser beam as the flow visualization system to produce the optical wavefront. A thin-film polarizer and a half waveplate were used to divide out a low energy portion of the beam. This beam was then further reduced in intensity using ND filters and the Fresnel reflection (back reflection) off of a prism. The beam was spatially filtered using a 10 micron pinhole and an 8 mm objective lens. The resulting, ~50 mm diameter, planar wavefront was then directed through the flow. A telescoping system consisting of a +500 mm and +150 mm lenses was used to image the wavefront onto the lenslet array. This magnified the wavefront tilts and increased the sampled area by a factor of 3.33. The lenses were located one focal length away from just beneath the flow and lenslet array, respectively, according to the requirements of Fourier optics to provide a 4-f relay system, thus negating propagation effects.

The lenslet array consisted of square lenslets with 328 micron pitch and 26 mm focal length. A DVC (model 1310-M) camera with 1300 x 1030 pixels was placed at the focal plane of the lenslet array. Each pixel is 6.7 microns square with a fill factor of close to 100%. A total of 26 x 21 spots were formed on the camera, with each spot measuring about 10 pixels in diameter. A 50 x 50 pixel region on the camera was dedicated to each spot and individual spots can be accurately located to less than 1/10th of a pixel. This results in a tilt sensitivity range of 23 to 3442 microradians for the sensor. Combined with the telescoping optics, each measured wavefront has dimensions of 28.4 mm x 23.0 mm with each lenslet sampling a 1.09 mm x 1.09 mm area. The longer dimension was aligned with the flow direction of the jet.

D. Simultaneous flow and wavefront measurement set-up and experimental conditions

Figure 2 presents a schematic of the SH sensor and flow visualization system set up for simultaneous measurements. The camera for flow visualization is not shown, but is placed perpendicular to the laser sheet. The rectangular jet nozzle is connected to a stagnation chamber with a ~1m pipe. The pressure was set for ideally expanded flow and maintained constant to within ± 2 %. An optical rail is mounted directly above the nozzle and forms the incident wavefront branch of the system. Neutral density (ND) filters, a spatial filter consisting of two lenses and a pinhole, and a turning mirror are mounted to the optical rail and serve to produce and direct a planar wavefront through the flow. Immediately below the nozzle, a breadboard was

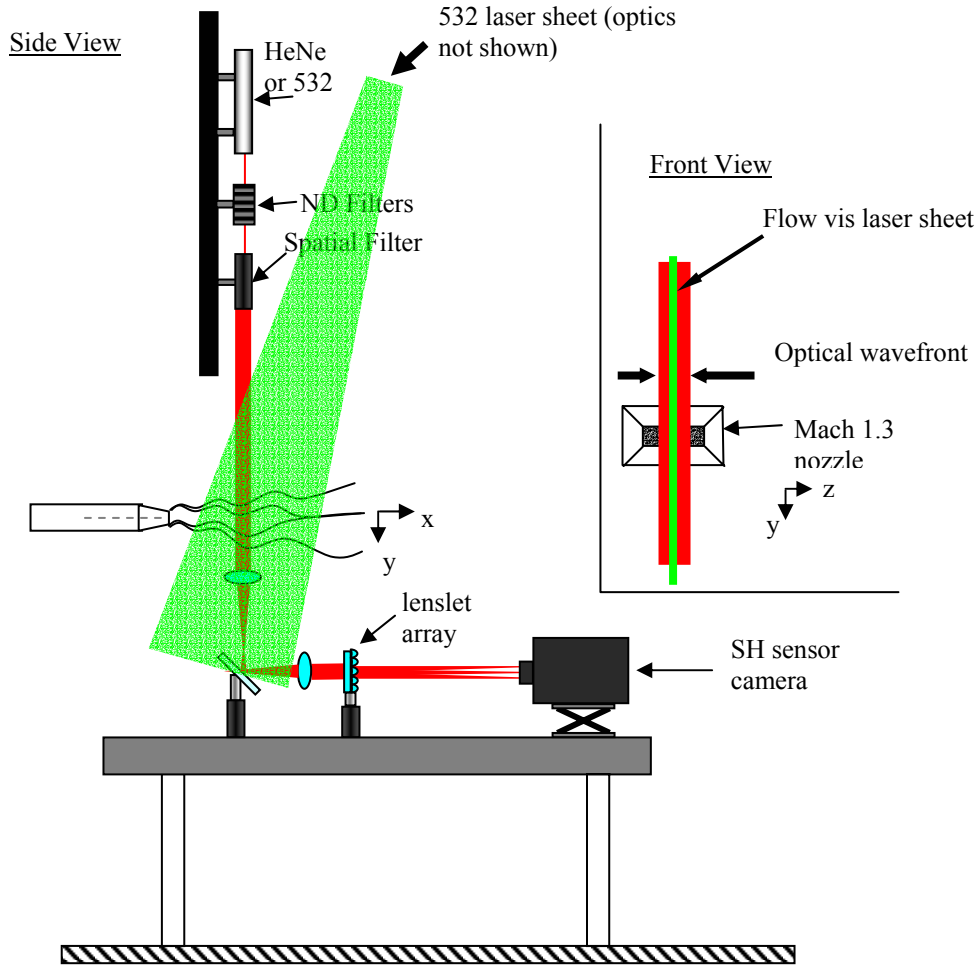


Figure 2 – Schematic of experimental arrangement.

positioned. Turning mirrors and telescoping optics were then appropriately placed to image the sampled wavefront onto the SH sensor.

The flow visualization branch of the system is set up on another optical rail parallel to the incident wavefront branch. To avoid any interference of the separate branches, the laser sheet was directed through the flow at an approximately 10 degree angle relative to the incident wavefront. The laser sheet is formed using a cylindrical lens to spread the beam out and a long focal length spherical lens to focus the beam into a thin sheet. Although the laser sheet and optical wavefront overlap through the flow, they are isolated from one another due to the difference in propagation directions and the addition of a polarizer not shown (the beams are polarized perpendicular to one another).

For these experiments data was taken in 5 sets. Each set consisted of 25-50 images and took approximately 2 minutes to run. There was approximately 5 to 15 minutes between each set. In addition, following the 5 sets, reference images were

acquired with the flow turned off to establish reference locations of the spots of the SH sensor. The location of these 'zero points' are compared with the location of spots measured with the flow on; the difference in position is then the displacement used in Eq. 1. In addition to streamwise images, some cross-stream images were acquired using the high resolution flow visualization system. These images are used to show the three-dimensionality of the flow field.

IV. Index-of-refraction model

Flow visualization is a very useful tool for understanding the dynamics of turbulent flows. To relate flow images to the optical distortion of a wavefront that occurs as it passes through the turbulent flow, a model must be developed that relates the features in a flow image to the distorted wavefront. A preliminary model is presented here that shows some promise in representing the main effects of turbulence on an optical wavefront.

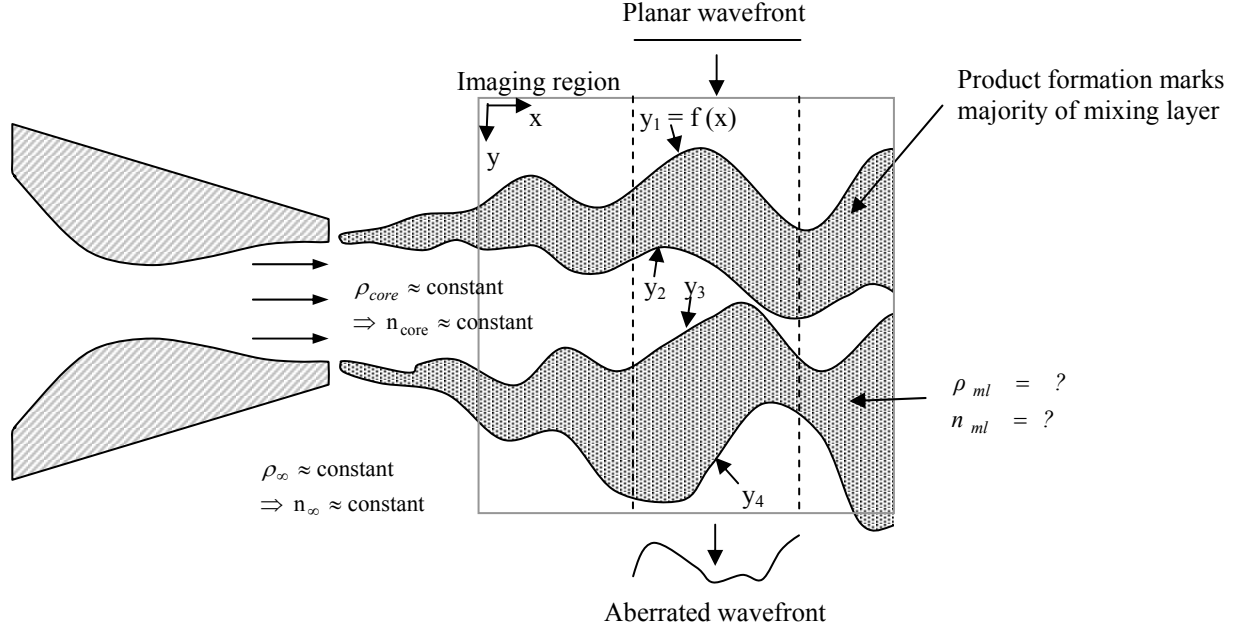


Figure 3 – Schematic of significant features of flow visualization index-of-refraction model.

Given an index-of-refraction field in three-dimensions and assuming small deflection angles (i.e. $\theta \ll 1$), the optical distortion of a planar wavefront traveling in the y -direction can be represented by the optical path length (OPL):

$$OPL(x, z) = \int_{y=-\infty}^{y=\infty} n(x, y, z) dy \quad (2)$$

Note that propagation is in the y -direction (in accordance with fluids conventions) and not in the z -direction (optics convention). The two dimensional OPL $[=f(x, z)]$ represents a surface of constant phase. Typically, it is more convenient to express the distortion in terms of the optical path difference (OPD) defined as

$$OPD(x, z) = OPL(x, z) - \overline{OPL}(x, z) \quad (3)$$

where the overbar indicates the instantaneous spatial average. The index-of-refraction is related to the density of the flow through

$$n = 1 + K_{GD} \rho \quad (4)$$

where K_{GD} is the Gladstone-Dale coefficient ($K_{GD} \sim 2.26 \times 10^{-4} \text{ m}^3/\text{kg}$ for air). With Eqns. 2-4, the distortion of a wavefront can be computed directly from the three-dimensional density field of the flow.

Measurements within compressible flow fields, however, are typically limited to point or planar measurements with quantitative planar measurements being quite challenging and one-dimensional (spatially stationary) measurements being of limited use with respect to aero-optics. For this study, planar flow

visualization was used as the flow diagnostic. Thus, the challenge is to model the density of the flow from inherently qualitative images. Furthermore, the free jet with the core of the jet sandwiched between an upper and lower half of the mixing layer makes this task even more challenging. As the flow information is only contained in two-dimensions (x & y ; Fig. 2), the integral in Eqn. 2 reduces the corresponding wavefront to one dimension:

$$OPL(x, z = z_0) = OPL(x) = \int_{y=-\infty}^{y=\infty} n(x, y) dy \quad (5)$$

In order to estimate the index-of-refraction field contained in a flow visualization image, it is important to understand exactly what is being visualized in the flow images. As stated, product formation is used to generate laser light scattering particles in the flow. In this technique, particles are formed when warm, moist ambient air is entrained into the jet and mixed with cold and dry jet core air. Thus, particles are formed in regions of the flow where mixing has occurred, where the temperature is low enough for water condensation and where these conditions have been met for a long enough time for water droplets to grow and produce a significant scattering cross-section. Obviously, this is a very complex problem to analyze. It is reasonable to assume, however, that product formation marks the majority of the mixing layer. A product formation technique using ethanol instead of water was studied in

detail by Messersmith et al. (1991) and it was concluded for their experimental set-up that product formation produced a large enough number density of light-scattering particles for mixture fractions ranging from 0.2 to 0.8. This may be considered the worst case for this experiment as they assumed a dynamic range for their detector of approximately 100:1. In the current experiments, however, the dynamic range is approximately 5000:1 due to recent advances in CCD technology. Thus, we may conclude that the signal in the current images marks a very large and significant portion of the mixing layer and that the size and shape of structures may be inferred from the images.

With this in mind, Figure 3 is presented. This figure schematically shows the decomposition of the flow images into three regions with four surfaces as the boundaries. The three fluid regions are 1) ambient; 2) jet core; and 3) mixing layer, properties of which are shown with subscripts ∞ , core, and ml, respectively. In the figure, the optical wavefront to be measured passes approximately through the center of the image. Initially, the wavefront is propagating (top to bottom) through the ambient air. The ambient air will be quiescent, except for the entrainment into the jet with quite low velocity, and the density will be constant. Thus, the index in this region of fluid is spatially invariant:

$$n_{\infty} = 1 + K_{GD} \rho_{\infty} = \text{constant} \quad (6)$$

After some distance, the wavefront will begin to propagate through the mixing layer. In reality, the transition from ambient conditions to turbulent conditions in the mixing layer will be continuous. In the model, the transition is represented as a discrete boundary by the line $y_1=f(x)$. The location of this line can be determined directly from the intensity in the images. The density within the mixing layer is a function of position and is represented as

$$n_{ml}(x, y) = 1 + K_{GD} \rho_{ml}(x, y) \quad (7)$$

where $\rho_{ml}(x, y)$ is undetermined for the time being.

Following passage through the mixing layer, the wavefront will enter into the jet core [marked by the line $y_2=f(x)$]. Again, the transition in reality will be gradual. Assuming an ideally expanded jet, the core fluid will have nearly uniform properties throughout and thus its index-of-refraction will be assumed spatially invariant

$$n_{core} = 1 + K_{GD} \rho_{core} = \text{constant} \quad (8)$$

Equation 5 can thus be written in the following form

$$OPL(x) = \int_{y=-\infty}^{y=y_1(x)} n_{\infty} dy + \int_{y=y_1(x)}^{y=y_2(x)} n_{ml}(x, y) dy + \int_{y=y_2(x)}^{y=y_3(x)} n_{core} dy + \int_{y=y_3(x)}^{y=y_4(x)} n_{ml}(x, y) dy + \int_{y=y_4(x)}^{y=\infty} n_{\infty} dy \quad (9)$$

where n_{ml} is yet to be determined.

As discussed earlier, the prospects for determining n_{ml} directly from the images is poor due to the complex physics involved. Rather, we propose that n_{ml} can be represented by a mean value, \bar{n}_{ml} , that represents the net effect of the mixing layer. Mathematically, this is

$$\bar{n}_{ml} = \frac{1}{A_{ml}} \iint_{A_{ml}} n_{ml} dA \quad (10)$$

where \bar{n}_{ml} is the average of the index-of-refraction through the entire mixing layer.

Accounting for the discretized form of the image, Eq 9 becomes

$$OPL(x) = \sum_{y=1}^{y=y_1(x)} n_{\infty} \Delta y + \sum_{y=y_1(x)}^{y=y_2(x)} \bar{n}_{ml} \Delta y + \sum_{y=y_2(x)}^{y=y_3(x)} n_{core} \Delta y + \sum_{y=y_3(x)}^{y=y_4(x)} \bar{n}_{ml} \Delta y + \sum_{y=y_4(x)}^{y=N} n_{\infty} \Delta y \quad (11)$$

where Δy is the image resolution and N is the number of pixels in the y direction. \bar{n}_{ml} is a single value that has not been determined and must be determined experimentally.

Dimotakis et al. (2001) proposed a similar representation of the flow field for an incompressible planar shear layer. Their observation was based on Rayleigh scattering measurements made in a flow field consisting of two dissimilar index-of-refraction gases. They found that the mixing layer's index of refraction could be represented by the average mixture fraction within the mixing layer. As differences in the index-of-refraction is quite small in the current experiments, we define a normalized index, \hat{n}_{ml} , as

$$\hat{n}_{ml} = \frac{\bar{n}_{ml} - n_2}{n_1 - n_2} \quad (12)$$

where the subscripts 1 and 2 represent the high and low-speed streams, respectively. For the current experiments $n_1=n_{core}$ and $n_2=n_{\infty}$. For the incompressible case of Dimotakis et al., this value was experimentally determined to be ~ 0.53 . The applicability of this value/model to compressible, single constituent flow-fields, however, was not discussed and is need of further exploration.

The validity of the proposed model for a compressible flow field is one of the issues explored in this paper. As will be discussed, the model is found to produce waveforms consistent with those measured directly, albeit using different values for \hat{n}_{ml} than the incompressible value given by Dimotakis et al. This will further be discussed in the presentation of the results. Further development of the model is currently under way.

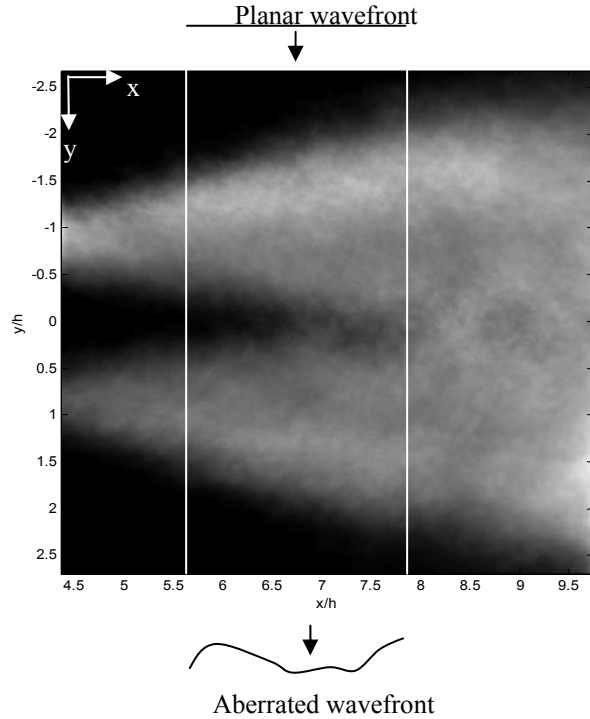


Figure 4 – Average streamwise flow visualization image. Vertical lines indicate passage of optical wavefront through the flow.

V. Results

Figure 4 is an average streamwise image of the flow field and is based on 148 images. The two vertical lines indicate the region where the optical wavefront was passed through before it was measured by the SH sensor. Keep in mind that the measured wavefront extends into and out of the page as well. Figure 5 is an average of 150 cross-stream images taken at $x/h=7$ (approximately in the middle of the wavefront aperture) and gives a picture of the three dimensional structure of the mixing layer. Again, the vertical white lines indicate the location of the passage of the optical wavefront on the y - z plane, which passes approximately through the center of the flow field.

Figure 6 is the average two-dimensional wavefront created from 128 instantaneous wavefronts as measured by the SH sensor. The OPD is measured in terms of waves (ϕ/λ) with $\lambda=1315$ nm. This wavelength was chosen as it is the wavelength of the COIL laser currently for the Boeing airborne laser platform. The overall features of the average wavefront match quite well with the features of the average images. The optical path length is lower at the spanwise edges of the wavefront. In these regions, as seen in Figure 5, both the jet core and mixing layer are

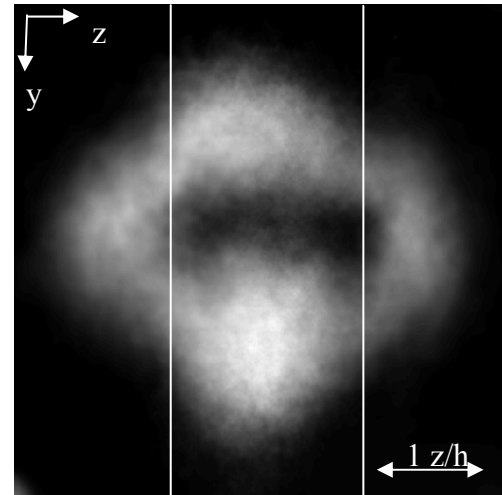


Figure 5 - Average cross-stream flow visualization image. Vertical lines indicate passage of optical wavefront through the flow. Laser sheet had non-uniform intensity and was brighter on bottom half of mixing layer.

smaller in size than at the center of the jet. The extent of these regions grows with downstream distance as the jet core shrinks. Figure 4 demonstrates the reduction in jet core size with downstream distance. The jet core has a higher index-of-refraction and, therefore, a longer relative optical path length. As these regions become smaller, so too does the optical path length.

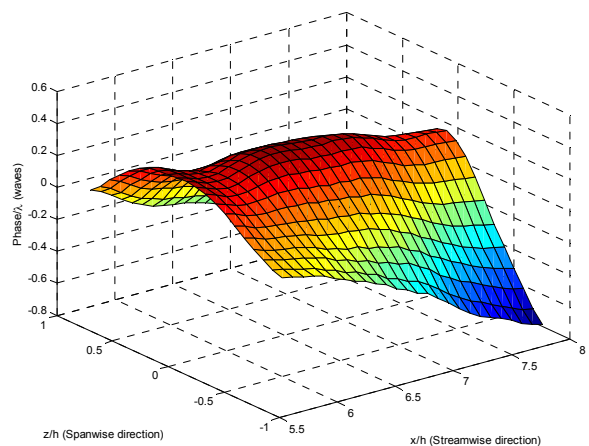


Figure 6 – Average optical wavefront. $\lambda = 1315$ nm.

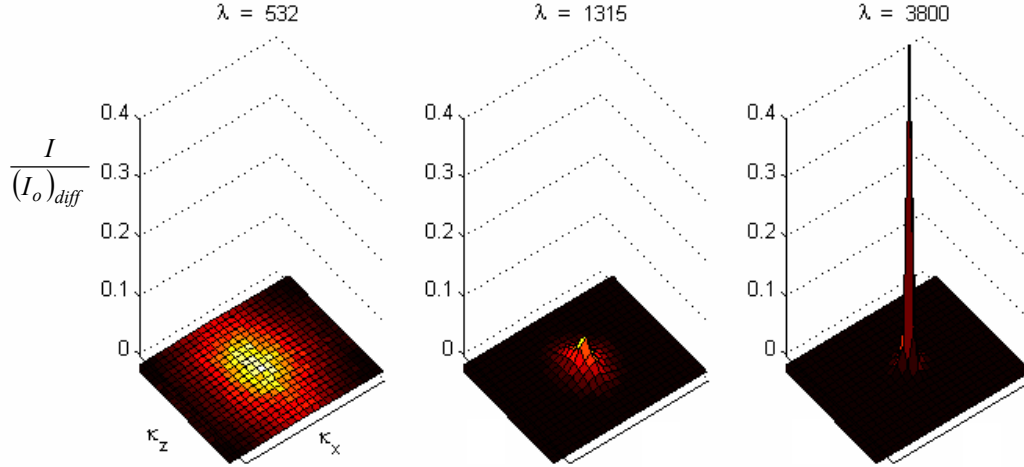


Figure 7 – Average point spread function for $\lambda = 532$ (Nd:YAG), 1315 (COIL) and 3800 nm (DF).

A useful measure when considering optical wavefronts is the point spread function (PSF). The point spread function is the intensity pattern that a planar wave would have at the focal point when passing through a lens and is a good measure of the effects of turbulence on the wavefront. The PSF is computed from the instantaneous wavefronts through

$$PSF(\kappa_x, \kappa_z) = |F(\kappa_x, \kappa_z)|^2 \quad (13)$$

where $\kappa_x = (2\pi x / \lambda f)$, f being the focal distance, and $F(\kappa_x, \kappa_z)$ is the Fourier transform of the near field complex field, $G(x, z)$ given by

$$G(x, z) = \exp(j \frac{2\pi}{\lambda} \phi(x, y)) \quad (14)$$

where ϕ is the phase of the wavefront measured (by the SH sensor) in units of length. Here, the electric field across the wavefront is assumed to have a magnitude of unity and only the phase varies.

The average point spread function of the aberrated wavefronts is shown in Figure 7 for three different wavelengths. The advantage of the SH sensor is in its ability to capture general wavefront information that can be analyzed at different wavelengths of light than that used in the experiment. The wavefronts were acquired with 532 nm light, but PSFs are computed for wavelengths of 532, 1315 and 3800 nm, which correspond to the wavelength of a frequency doubled Nd:YAG, COIL and DF lasers, respectively.

The loss of on-axis intensity is quite clear from the figure as the PSF is quite broad for the lower wavelengths. This reduction in intensity is measured through the Strehl ratio (SR), which is the ratio of the on-axis intensity to the diffraction limited, aberration free intensity ($I/I_{o, \text{diff limited}}$). For $\lambda = 532$ nm, the average PSF is quite spread out and has an $SR < 0.01$. At

$\lambda = 1315$ nm, $SR \sim 0.04$ and for $\lambda = 3800$ nm, it is about 0.4. The peak intensity of many of the PSFs, however, occurs at an off-axis location. Taking the ratio of the peak intensity (as opposed to the on axis intensity) to the diffraction limited values, the Strehl ratios become 0.02, 0.11, and 0.55, respectively.

Note that the PSF calculations presented in Figure 7 do not take into account any other effects (e.g. atmospheric effects) than the wavefront distortion due to the flow (i.e. aero-optic effects). While the flow field in the current study does not represent the actual flow field over an aircraft, it does give an idea as to the nature of the problems associated with compressible flow fields and the dependency on the wavelength of light.

The ultimate goal of aero-optic studies is to devise an adaptive optic or flow control technique that will minimize the optical distortion that occurs due to the flow field. To proceed in this direction, the instantaneous details of the flow and associated wavefronts must be known to better characterize the problem. In this set of experiments, simultaneous measurements of the flow and wavefronts were conducted. The development of flow control techniques, however, is typically conducted without consideration of the aero-optic distortion that will occur. To bridge the field of aero-optics with recent developments in flow control, a simple and straight forward model relating flow visualization images to aero-optical distortion would be quite useful. This would allow researchers to adapt their flow control techniques based on flow visualization data and still have an idea of how it might impact aero-optics. The development of this model becomes increasingly difficult, however, as one tries to incorporate the effects

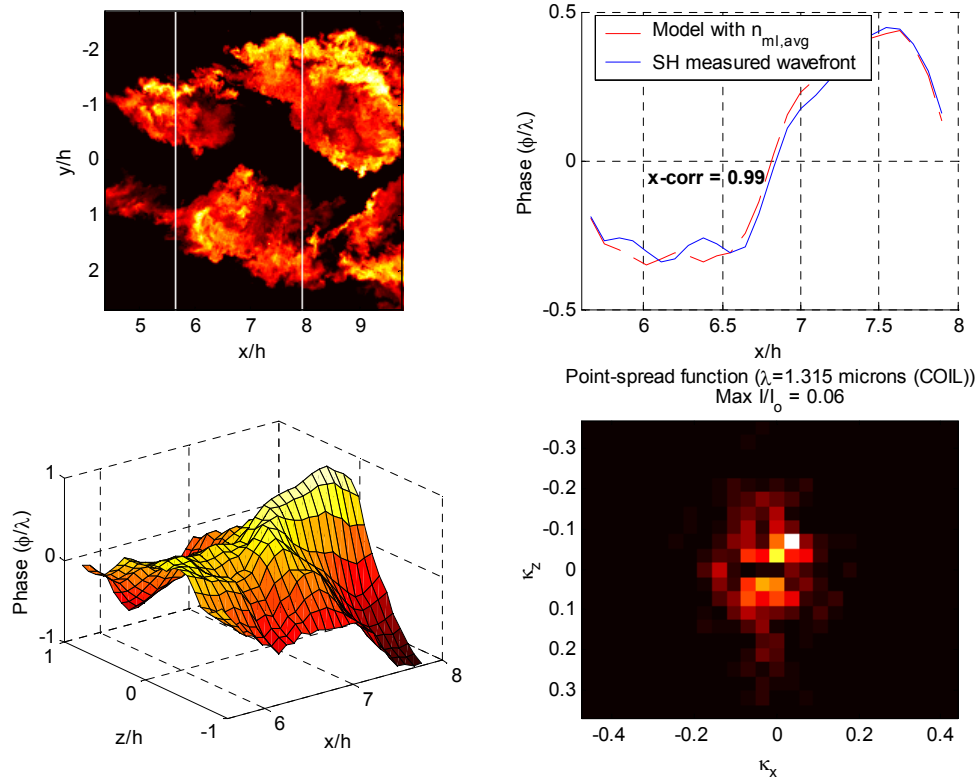


Figure 8 – Simultaneous measurement of mixing layer and optical wavefront.

Upper left: Flow visualization image.

Lower left: Optical wavefront measured with SH sensor.

Upper right: Comparison of modeled wave with $\hat{n}_{ml}=0.38$ (computed from flow visualization image)

and measured wave (slice of lower left taken at $z/h \sim 0$).

Lower right: PSF of optical wavefront in lower left.

of compressibility into it. With this said, the results presented here are part of an on-going effort to relate the features of compressible shear layers to the optical distortion that occurs during the passage through them.

Details of the model were described in Section IV. As mentioned, the model is based on the idea of representing the shear layer with an average value of the index-of-refraction. This value will subsequently be reported by the normalized index:

$$\hat{n}_{ml} = \frac{\bar{n}_{ml} - n_{\infty}}{n_{core} - n_{\infty}}$$

In Section IV, \hat{n}_{ml} was left undetermined. Note that for \hat{n}_{ml} a value of zero and one would represent a uniform flow with an index of refraction similar to the ambient and the jet core, respectively. As both the wavefront and the flow are measured simultaneously, \hat{n}_{ml} can be

calculated from the data for each image/wavefront pair. This was accomplished using an iterative scheme to minimize the error between the modeled wavefront (calculated from the flow visualization images and the model) and the measured wavefront (from the SH sensor).

Figure 8 is a particularly good example of the comparison of the model with the SH sensor result. The flow visualization image is shown in the upper left corner of the figure. White vertical lines indicate the passage of the optical wavefront through the flow. Immediately below the image is the two-dimensional wavefront measured by the SH sensor. To the right of the wavefront, the PSF calculated from the wavefront is shown (units given in mm^{-1} , see Eqn. 13). In the upper right corner, the one-dimensional wavefront determined from the model and the image is compared with a one-dimensional slice taken from the two-dimensional



Figure 9 – Sample of instantaneous cross-stream image for Mach 1.3 rectangular jet.

wavefront data at $z/h=0$. Keep in mind that the two-dimensional wavefront in the lower left is a product of the three-dimensional flow field. Here, we are only able to visualize a two-dimensional plane within the flow field. Thus, the flow model can only reconstruct a single dimension of the optical wavefront.

Taking a closer look at Figure 8 reveals that the flow is quite three-dimensional. This is evident in the two-dimensional phase front which is marked by a large ridge running through its center. The two-dimensional nature of the wavefront is manifested in the PSF which indicates a broadened intensity profile with a peak intensity of only 6% of its diffraction limited value. In addition, the peak intensity occurs at an off-axis location (beam steering). The three-dimensionality of the flow field is better represented by a typical instantaneous cross-stream image presented in Figure 9 (taken at a different time). In this image, the flow is clearly highly three-dimensional on an instantaneous basis. Thus, the streamwise image shown in the upper left of Figure 8 is not indicative of the entire flow field and the extent of structures into and out of the page is unknown.

In the example presented in Figure 8, the modeled wavefront most accurately matched the

measured wavefront for a value of $\hat{n}_{ml}=0.38$. The accuracy of this fit is indicated by a cross-correlation coefficient of 0.99. The cross-correlation coefficient is a mathematical representation of the similarities between two signals. In this case, a value of 1.0 would represent perfect correlation (identical waveforms) between signals and a value of -1.0 would represent perfect anti-correlation (i.e. conjugate waveforms). The high level of correlation for the waveforms of Figure 8 indicates a very good match between the modeled wavefront and the measured wavefront. Physically, the value of 0.38 for \hat{n}_{ml} implies that the average index-of-refraction (and, therefore, density) is slightly closer to the ambient value than the jet core value for this case. At this point, however, the reader is cautioned against this line of thinking for reasons to be discussed later.

The value of \hat{n}_{ml} will vary from image to image. In Figure 10 \hat{n}_{ml} has an optimal value of 0.03. Again, the correlation level is quite good at 0.96. The flow visualization image appears to be void of signal in some of the regions between each of the large-scale structures. There is enough signal, however, within these regions to distinguish the mixing layer from the background, thus allowing for the application of the model to the image.

Within each individual set of data (total of 5 sets of 25-50 image/wavefront pairs each), the optimal value varied from the mean with a standard deviation of ~ 0.25 . A histogram of values for \hat{n}_{ml} over all 5 datasets is shown in Figure 11. The spread of values is centered at ~ 0.16 .

Figure 10 also demonstrates some other interesting features about wavefronts passing through this turbulent flow field. The two-dimensional wavefront of Figure 10 is much smoother and varies less than the wavefront in Figure 8. This is further reflected in the PSF which shows the energy of the focused beam contained in a much smaller area. The maximum normalized intensity in this case is 0.18, which is three times higher than the previous example. This is in spite of what appears to be a very organized pattern of vortices in the mixing layer. The vortex on the top is quite large with distinct small braid regions; there is also a very identifiable asymmetric pattern with the lower half of the mixing layer.

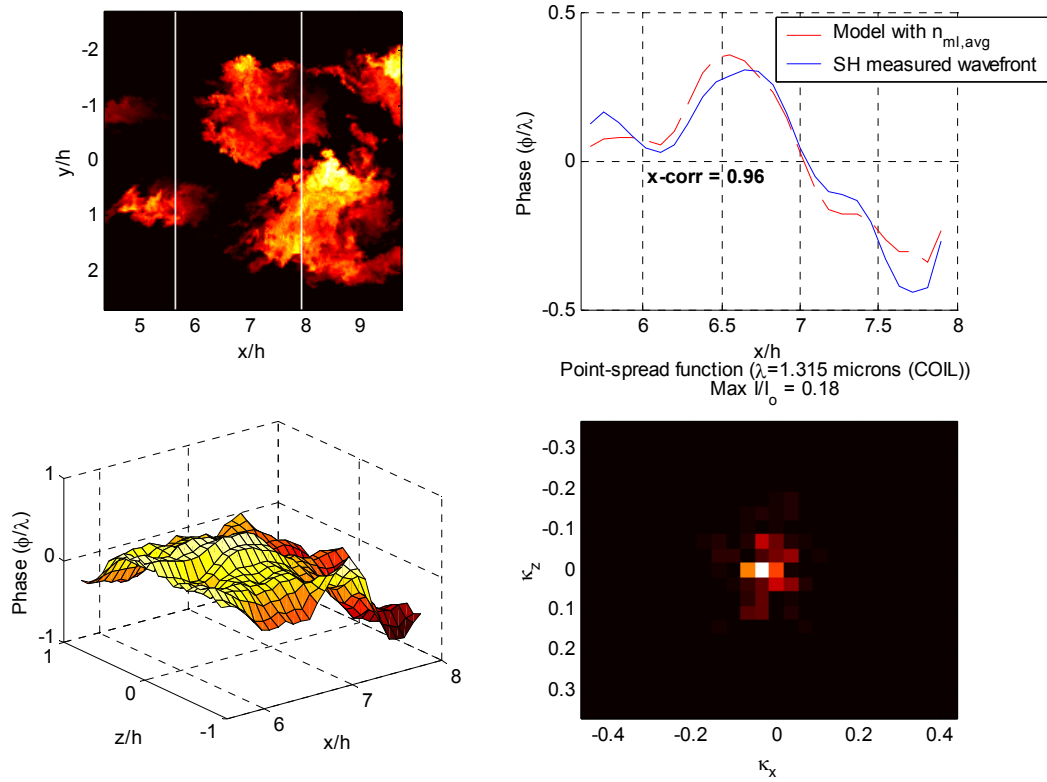


Figure 10 – Simultaneous measurement of mixing layer and optical wavefront.

Upper left: Flow visualization image.

Lower left: Optical wavefront measured with SH sensor.

Upper right: Comparison of modeled wave with $\hat{n}_{ml}=0.03$ (computed from flow visualization image)

and measured wave (slice of lower left taken at $z/h=0$).

Lower right: PSF of optical wavefront in lower left.

Figures 8 and 10 indicated an extremely high level of correlation between the modeled wavefronts and the measured wavefronts. These figures, however, are some of the better examples. In general, the degree of correlation varies, but is still fairly high for most cases. Figure 12 is a histogram of all the cross-correlation values obtained between the modeled and measured wavefronts found in these experiments (128 total). The average value is 0.73 while the median value is 0.84. Clearly, there is a good agreement between the modeled and the measured wavefronts.

Figure 13 is presented to give the reader a better feel for the physical significance of the cross-correlation coefficient. In this case, the cross-correlation value is 0.71, just below the average value. Approximately 70% of all image/wavefront pairs have a higher correlation value. The cause of the lower value of correlation is quite clear as the shape of the wavefronts do vary relative to one another. The general shape of the modeled wavefront, however, does agree

fairly well with the measured wavefront. Interestingly, it appears that a small shift in x-location might lead to a better matching between the two wavefronts.

VI. Discussion

The main intent of this work was to explore the application of MHz rate optical diagnostics to aero-optics. A preliminary work demonstrated their potential, but lacked the details to truly characterize their capabilities. As such, experiments were conducted to gain a higher quality understanding of the challenges associated with aero-optic applications.

A major part of this challenge is the establishment of a flow model that can objectively tie together observations made from planar flow visualization with measurements from a SH sensor. The development of a suitable model will allow for more flexibility in future experiments and should alleviate the need for an overwhelming suite of

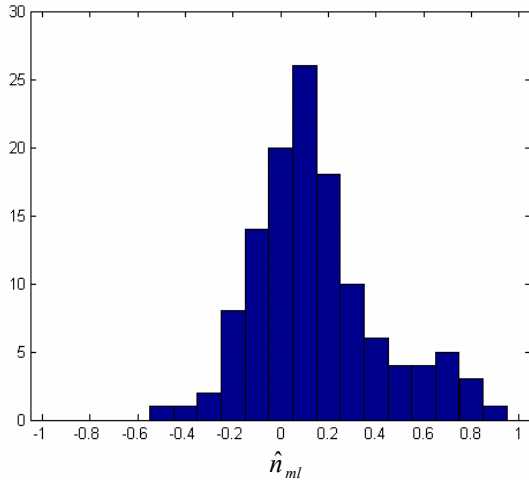


Figure 11 – Histogram of calculated values for \hat{n}_{ml}

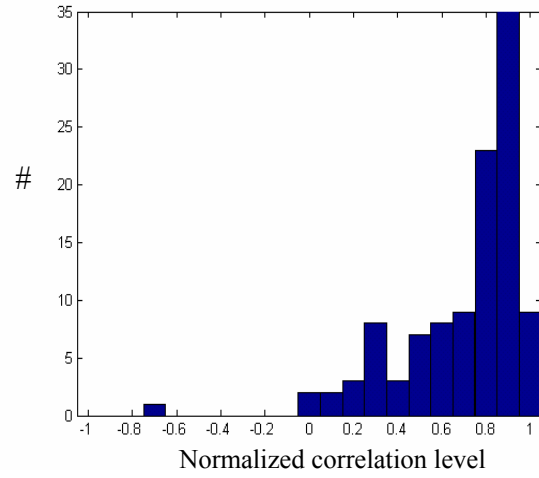


Figure 12 – Histogram of normalized correlation values between measured and modeled wavefronts.

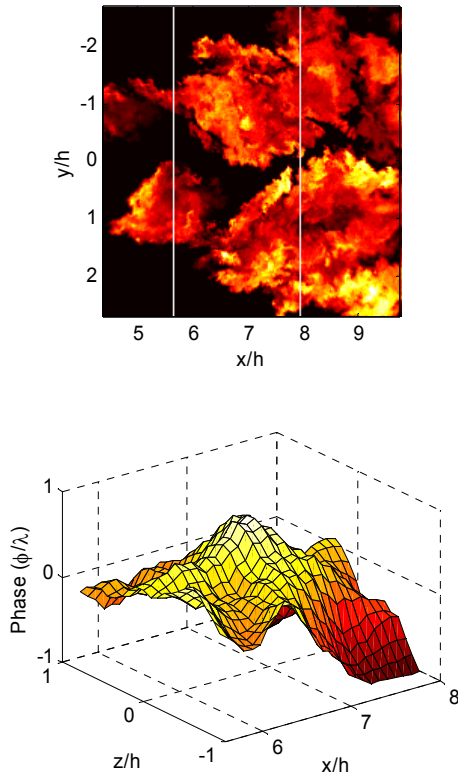


Figure 13 – Simultaneous measurement of mixing layer and optical wavefront.

Upper left: Flow visualization image.

Lower left: Optical wavefront measured with SH sensor.

Upper right: Comparison of modeled wave with $\hat{n}_{ml}=0.08$ (computed from flow visualization image) and measured wave (slice of lower left taken at $z/h \sim 0$).

Lower right: PSF of optical wavefront in lower left.

experimental techniques required to explore basic and fundamental aero-optics issues. In light of this, the preliminary model proposed should be considered a start in the right direction.

As evidenced by the three image/wavefront pair examples of Figures 8, 10 and 13, the modeled wavefronts agree quite well with the measured wavefronts. This is further supported in Figure 12 where half of the image/wavefront pairs had cross-correlation values greater than 0.84. Based on these results, the simple concept that the mixing layer can be represented by a single average value, \hat{n}_{ml} , of the index of refraction is quite encouraging. The range of values measured for \hat{n}_{ml} and shown in Figure 11, however, makes the application of this model to other flow visualization images challenging as there is not a universal value for the flow field. In addition, the model does not distinguish between various scales and structures within the mixing layer. A model that incorporates more information about the dynamic details of the mixing layer would be more accurate and applicable to a much broader range of experimental data. With these items in mind, we continue by exploring a few shortcomings of the current model and discussing some details that will be addressed in future works on the subject.

There are a number of reasons that the modeled wavefront may not agree with the SH measured wavefront no matter how accurate the model is. For one, the location of the spots formed on the CCD chip by the lenslet array can only be determined to an accuracy of approximately 0.1 pixels. In the current experiment, this can result in a tilt measurement error of ~ 23 microradians or about 0.006 waves over each lenslet aperture. Secondly, each lenslet in the lenslet array produces a displaced spot that is the cumulative effect of the turbulent features within a finite volume of the flow. The plane being visualized in the flow has a depth of approximately 0.1 mm (laser sheet waist thickness). Each spot, however, represents a wavefront area of $\sim 1.1 \times 1.1$ mm. Thus, any out-of-plane three-dimensionality of the flow will not be observed in the flow visualization images, but will be represented in the SH measured wavefront. For example, the wavefronts in Figure 13 appear to be similar except for a small shift in position. An oblique large-scale structure could potentially cause such a shift. From this point of view, however, the high resolution flow visualization images may be able to produce a higher resolution wavefront through the model than the SH sensor, albeit only in one dimension.

Another limitation, and perhaps the most significant one, to the current set of results is the flow geometry. As seen in the images, structures within the mixing layer of a rectangular jet exhibit an asymmetric

pattern with structures on either side of the mixing layer. The presence of an upper and lower half of the mixing layer makes it much more difficult to deduce the effect of individual structures on an optical wavefront. Rather, the asymmetric pattern of the mixing layer curtails the impact of an individual structure as structures and their braid regions are overlapping. Thus, the results presented here are going to be the integrated effect of large-scale structures and their braid regions from both halves of the mixing layer and not any one structure in particular.

The geometry of these experiments, however, was chosen for convenience and availability, not necessarily aero-optic applicability. Currently, a new facility is being designed that will allow for a greater flexibility in flow geometries that will better represent typical aero-optic flows. For example, the facility will allow for the investigation of a planar shear layer. This geometry will effectively isolate the effect of individual turbulence structures from one another and allow for a more detailed investigation into the aero-optic effects of individual structures. Accounting for individual structures will have a much more general and broader impact on future possibilities involving flow control. These details may also help explain the variation in \hat{n}_{ml} observed.

As demonstrated in Figure 11, the value of \hat{n}_{ml} can vary substantially from one image to another with an average value of 0.16. If the flow within the mixing layer were homogeneously and isentropically mixed (not necessarily a correct assumption), \hat{n}_{ml} should have a value of 0.5. Inhomogeneity would lead to a variation in this value as observed. A large portion of the variation shown in Fig. 11, however, is felt to be due to the experimental procedure used. One explanation for the shift to lower values of \hat{n}_{ml} is the connection between the linear growth rate of the mixing layer and an error source within the SH sensor.

The mixing layer thickness, on average, increases linearly with downstream distance. This is reflected in the average flow visualization image of Figure 4. By raising the value of \hat{n}_{ml} , the modeled OPD in the downstream direction increases proportional to the mixing layer thickness. Thus, raising \hat{n}_{ml} has the effect of adding a constant tilt to the modeled wavefront in a counter-clockwise direction. On an instantaneous basis, the mixing layer does not grow linearly; rather, it contains a multitude of structures of varying size. Still, the trend is a general increase in mixing layer thickness with downstream distance.

Conversely, a tilt of the measured wavefront can also occur if the CCD camera of the SH sensor were to move in time relative to the lenslet array (such

as a settling of a translation stage or mounting piece). In the current experiments, a set of reference spot locations (no flow) was acquired at a separate time than the displaced spots (flow on). If the camera were to move between these acquisition times, the movement would cause each spot of the SH sensor to be displaced by a fixed value. This would, in turn, cause each tilt measurement to be biased by a constant value. For example, if the lenslet array shifted 1 micron relative to the SH camera, this added spot displacement would result in an added measured tilt of 34 microradians across each lenslet. In the wavefronts shown, this corresponds to a constant increase in OPD of .008 waves over each lenslet for a total of ~ 0.22 waves over the entire wavefront. The general shape of the measured wavefronts, however, will be the same except they will be tilted (analogous to rotation). For the experimental method used here, a small shift would be difficult to detect.

The data presented here was taken in 5 sets of 25-50 image/wavefront pairs each with the reference ('zero point') locations taken after the last set. Each set took approximately 2 minutes to acquire the data, but a larger amount of time existed between each set. The average value of \hat{n}_{ml} ranges from ~ 0 for the first set to ~ 0.35 for the last set. To assess the possible movement of the camera relative to the lenslet array with time, the average value of \hat{n}_{ml} for each set of data was plotted vs. the time that the data was acquired. This is shown in Figure 14. The value of \hat{n}_{ml} appears to grow linearly in time. These results seem to be consistent with the idea of a translation stage or mounting device constantly settling over time. This type of movement would be slight and difficult to detect. If this settling movement were linear, and one were to project the data to the time where the reference points were acquired, the average value of \hat{n}_{ml} would be approximately 0.5, an interesting result. An easy way to avoid this type of error in the future would be to incorporate reference point measurements into the procedure for every data set taken. This could be implemented simply by turning the flow off during the acquisition procedure and allowing a few extra wavefront/image pairs to be acquired without any flow. Thus the reference points would be acquired within seconds of the displaced spots.

Despite this complication, the proposed model appears to be a reasonable step in the right direction. The wavefronts and flow visualization images contain many large and undulating features that cannot be matched via the addition or subtraction of a simple tilt value. Even with the ambiguity of the reference point locations, the model reproduces very stark and pronounced features of the wavefront. The correlation levels are quite high for the entire data set. This

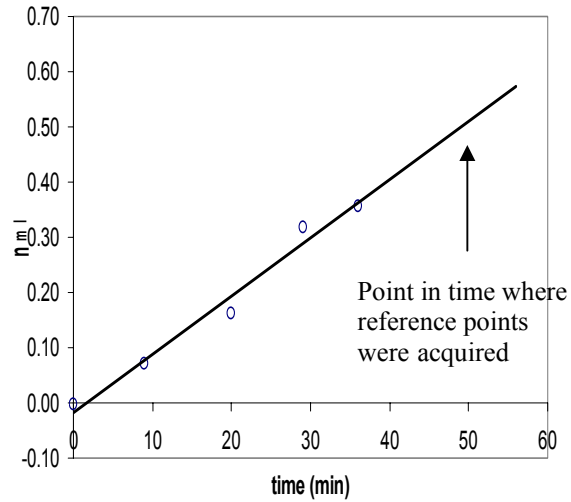


Figure 14 – Plot of average \hat{n}_{ml} for each set of data vs. time each set was acquired.

excellent agreement between the modeled wavefronts and measured wavefronts indicates that the modeling of the mixing layer with a single value of the index might be a good first approximation. Further investigation is needed, however, to determine a proper value for \hat{n}_{ml} for this flow field or any other flow field. Within each dataset, where any settling would be minimal, values of \hat{n}_{ml} still had a standard deviation of ~ 0.25 . This variation may be physical and needs to be explored in further detail.

VII. Conclusions

The results of this study indicate a strong correlation between the information contained in planar flow visualization images of a shear layer and the aberration of optical wavefronts passing through the shear layer. A preliminary index-of-refraction model for the flow visualization images was proposed and was quite successful at providing a link between flow visualization and wavefront measurements. Cross-correlation values between the modeled and measured wavefronts were well above 0.7 with an average value of 0.73 and a median value of 0.84. The encouraging development of this model will allow for a more detailed analysis of wavefronts in the time domain as MHz rate imaging and wavefront sensing are applied.

The main drawback to this study was the flow geometry of a rectangular jet. The presence of two halves of the mixing layer created an overlapping and asymmetric pattern of large-scale structures and their braid regions. Thus, the effects of individual structures could not be surmised. A more realistic and useful flow

model, however, would account for the variations in index that might accompany structures of various shapes and sizes. To proceed in this direction, a new facility is being designed that will have the flexibility to examine multiple flow situations. Initial experiments will be conducted on a planar shear layer at various convective Mach numbers. This will allow for a more thorough and detailed examination of the aero-optical effect of large-scale structures at various levels of compressibility. In addition, the facility is being designed with flow control in mind. Flow control will be used to change the nature of structures and, therefore, to develop a better understanding of how different structures play a role in aero-optical aberrations. Once a better understanding is achieved, flow control can then be applied to various practical geometries to achieve an aero-optics optimized flow field.

Acknowledgments

The support of this research by the DAGSI and AFRL is gratefully acknowledged. Fruitful discussion with Mike Stanek of AFRL is very much appreciated. The first author would like to thank the Department of Defense for his National Defense Science and Engineering Graduate Fellowship

References

- Dimotakis, P.E., Catrakis, H.J. and Fourguette, D. C., "Flow Structure and Optical Beam Propagation in High-Reynolds-Number Gas-Phase Shear Layers and Jets," *J. Fluid Mech.*, **433**, 105, (2001).
- Elliott, G. S., Samimy, M., and Arnette, S. A., "A Study of Compressible Mixing Layers Using Filtered Rayleigh Scattering," AIAA Paper 92-0175.
- Fitzgerald, E. J. and Jumper, E. J., "The Optical Distortion Mechanism in a Nearly Incompressible, Free Shear Layer," Under consideration for *J. Fluid Mech.*
- Hileman, J., Thurow, B. and Samimy, M., "Exploring Noise Sources Using Simultaneous Acoustic Measurements and Real-Time Flow Visualization in Jets," *AIAA J.*, **40**, 2382, (2002).
- R. J. Hugo, E. J. Jumper, G. Havener and C. Stepanek, "Time-resolved wave front measurements through a compressible free shear layer," *AIAA J.*, **35**, 671 (1997).
- Jumper, E.J. and Fitzgerald, E.J., "Recent advances in Aero-optics," *Prog. Aerospace Sci.*, **37**, 299. (2001)
- Kastner, J. and Samimy, M., "Development and Characterization of Hartmann Tube Fluidic Actuators for High-Speed Flow Control," *AIAA J.*, **40**, 1926, (2002).
- Kastner, J. and Samimy, M., "Effects of Forcing Frequency on the Control of an Impinging High-Speed Jet," AIAA Paper 2003-0006 (2003).
- Messersmith, N. L., Dutton, J. C. and Krier, H., "Mie Scattering Measurements of Scalar Probability Density functions in Compressible Mixing Layers," AIAA Paper 91-1686.
- Raman, G. and Kibens, V., "Active Flow Control Using Integrated Powered Resonance Tube Actuators," AIAA Paper 2001-3024 (2001).
- Stanek, M, Sinha, N, Seiner, J., Pearce, B., and Jones, M., "High Frequency Flow Control – Suppression of Aero-Optics in Tactical Directed Energy Beam Propagation and the Birth of a New Model (Part I)," AIAA Paper 2002-2272, May 2002.
- Thurow, B., Hileman, J., Lempert, W., and Samimy, M., "A Technique for Real-time Visualization of Flow Structure in High-speed Flows," *Phys. Fluids*, **14**, 3449 (2002).
- Thurow, B., Samimy, M., Lempert, W., Harris, S. R., Widiker, J. and Duncan, B., "Simultaneous MHz Rate Flow Visualization and Wavefront Sensing for Aero-optics," AIAA Paper 2003-0684 (2003).
- Thurow, B., Hileman, J., Samimy, M. and Lempert, W., "Progress Towards Real-Time Planar Doppler Velocimetry," AIAA Paper 2003-0916 (2003).
- Thurow, B., Samimy, M., and Lempert, W., "Compressibility Effects on Turbulence Structures of Axisymmetric Mixing Layers," *Phys. Fluids*, **15**, 1755, (2003).